Monthly Notices
of the
ROYAL ASTRONOMICAL SOCIETY

MNRAS **499,** 2817–2825 (2020)
Advance Access publication 2020 October 2

doi:10.1093/mnras/staa3048

Periodic brightening of Kepler light curves: investigating the possibility of forward scattering due to dust clouds

M. A. M. van Kooten [1]★ M. Kenworthy [1] and N. Doelman[1,2]

[1]*Leiden Observatory, Leiden University, Niels Bohrweg 2, 2333 CA Leiden, the Netherlands*
[2]*TNO, Stieltjesweg 1, 2628 CK Delft, the Netherlands*

Accepted 2020 September 29. Received 2020 September 25; in original form 2020 April 24

ABSTRACT

Dedicated transiting surveys, such as the Kepler space telescope, have provided the astronomy community with a rich data set resulting in many new discoveries. In this paper, we look at eight Kepler objects identified by Wheeler & Kipping with a periodic, broad increase in flux, that look distinctly different from intrinsic star variability. We consider two physical phenomena as explanations for these observed Kepler light curves; the first being the classical explanation while the second being an alternative scenario: (i) tidal interactions in a binary star system, and (ii) forward scattering from an optically thin cloud around an exoplanet. We investigate the likelihood of each model by modelling and fitting to the observed data. The binary system qualitatively does a good job of reproducing the shape of the observed light curves due to the tidal interaction of the two stars. We do, however, see a mismatch in flux right before or after the peak brightness. We find that six out of the eight systems require an F-type primary star with a K-type companion with large eccentricities. At the same time, we find that optically thin discs, modelled using a Henyey–Greenstein phase function are also able to generate these broad brightening events. Five of the eight observed objects can be described with this new hypothesis in the absence of RV observations. As the other three are not well-described by the disc model, we conclude that they are indeed heartbeat stars.

Key words: surveys – planets and satellites: detection – binaries: eclipsing.

1 INTRODUCTION

With dedicated surveys and space telescopes such as Kepler (Borucki et al. 2010) and *TESS* (Ricker et al. 2015), thousands of exoplanet candidates have been found due to the high precision photometry achieved by these missions – tens of parts per million reported by Christiansen et al. (2012) for Kepler. The Kepler mission is a rich data source with light curves from hundreds of thousands of objects. We know that many physical processes can cause variations in a light curve and by closely studying them we might be able to better understand what is happening around a star. Motivated by finding signals in Kepler data not necessarily due to exoplanets, and to probe other astrophysical processes, recent work by Wheeler & Kipping (2019) has demonstrated a new automatic flagging algorithm that can extract periodic signals that were previously only detected through power-spectrum analysis and visual inspection. Their newly identified objects show mainly brightening of the measured light curves. In this work, we focus on eight of these objects and look at two different processes that could result in the increase in flux seen in the data over short periods of order 20 d.

In the Kepler data set more than one hundred heartbeat systems have been identified and studied to date with both light curve and radial-velocity data (Welsh et al. 2011; Thompson 2012; Beck et al. 2014; Shporer et al. 2016). Exciting and dynamic systems, they show a photometric signal even when there is no eclipse. The observed photometric signal is due to tidal distortion, heating, Doppler beaming, and other effects. In this paper, we first consider the increase in flux (De Cat et al. 2000; Fuller 2017) due to the tidal interaction of heartbeat systems; the accepted explanation for the observed brightening in light curves that have similar features in combination with radial-velocity measurements.

From the NASA Exoplanet Archive we also know of multiple exoplanets with orbital periods of the order of 20 d – similar to the periods of the objects we consider in this paper. In some cases, such as Brogi et al. (2012) and Lamers, Lecavelier Des Etangs & Vidal-Madjar (1997), there is a slight increase in light before or after the transit event hidden among the star's own intrinsic variability – further complicating the light-curve analysis, and indicating certain phenomena are potentially being detected for the first time. We also expect a high number of grazing events of exoplanets in the Kepler data as any system orientation is equally likely compared to an observer. Observations of PDS70 have revealed the presence of circumplanetary discs around both PDS70-b (Christiaens et al. 2019) and PDS70-c (Isella et al. 2019). Andrews et al. (2018) show there are many protoplanetary discs with various geometries. Finally, Ansdell et al. (2016) detect a protoplanetary disc around 10 young late-K and M dwarf stars. We, therefore, consider an alternate model where forwards scattering from a cloud of dust results in a brightening in the light curve. The cloud of dust could be enshrouding an exoplanet. Or

★ E-mail: mvankoot@ucsc.edu

Table 1. Summary of the Kepler systems used in this work, including their Kepler magnitudes (K_p), orbital periods ($P_{\rm orb}$) determined in this work, and the number of Kepler quarters available for each target. The amplitude and errors are the relative flux as defined by Wheeler & Kipping (2019) and provide an estimation of the confidence of the signal.

KIC ID	K_p [mag]	$P_{\rm orb}$ [d]	Amp [ppt]	Amp error [ppt]	# quarters
7837214	13.95	7.49	0.99	0.04	17
11397541	9.98	13.25	0.96	0.02	18
6862114	8.01	27.68	0.62	0.03	18
4371947	12.28	19.72	0.36	0.02	15
8694536	12.33	35.95	0.28	0.01	18
7870350	12.26	23.142	0.35	0.01	18
10737327	12.12	22.78	0.22	0.02	17
11498661	14.18	42.09	0.35	0.03	18

alternatively, it could be a protoplanetary disc with gaps and specific geometry such that the observed brightening is produced due to the inclination of the system.

The rest of the paper is structured as follows; in Section 2, we describe the eight objects seen in the Kepler data and explain the data reduction performed. We then consider brightening due to tidal interaction of a binary star system, in Section 3. The results from fitting to this model are presented in Section 3.2. We then investigate forward scattering from an optically thin disc in Section 4 and show the results from fitting to such a model in Section 4.2. We discuss and compare the results from both models in Section 5. Lastly, we summarize our results and conclusions in Section 6.

2 OBJECTS OF INTEREST: KEPLER DATA REDUCTION AND ANALYSIS

We look at the previously unknown periodic signals detected by the non-parametric detection algorithm of Wheeler & Kipping (2019). Of these 18 previously unreported periodic objects, we look at the eight objects detected with high confidence. Table 1 contains the Kepler identification numbers, the Kepler magnitudes, and the periods determined in this work as well as the number of available Kepler quarters for which data was taken for the given object. Using the PYTHON package LIGHTKURVE (Lightkurve Collaboration 2018), we process the Kepler data. We make use of the pre-search data conditioning SAP flux (PDCSAP) generated by the Kepler Data Processing Pipeline which has removed long term trends using co-trending basis vectors (Smith et al. 2012). Note that we do not need to filter specifically for the long-cadence exposure time since the orbital periods of our objects are sufficiently long enough – of the order of tens of days. We combine the Kepler data for all quarters available by stitching them together after normalizing them. Then we remove all nan values and any outliers that are 5σ above the median flux using sigma-clipping. Finding the periodogram of the data, we determine the period by finding the maximum power for a frequency that is greater than 12 h (in order to avoid any intrinsic stellar variations) and fold the data on the identified periods, generating light curves as a function of orbital phase. The light curves are then binned by a factor of 5 in the orbital phase using the mean value. To have confidence in folded light curves, we repeated the above steps three additional times by randomly selecting three Kepler quarters each time. Doing so, we retrieve the same light curve shape and period. The periods we identify also agree with the periods found by Wheeler & Kipping (2019). For reference, the individual light curves of our systems are shown in Fig. 1 with the individual behaviour of the periodic signal from all the Kepler quarters. The folded light curves from combining all the available quarters are shown in Fig. 2. In all the light curves, we see a brightening over a large portion of the orbital phase. In the next sections, we consider two different explanations for the observed brightening.

3 BRIGHTENING DUE TO TIDAL EFFECTS IN BINARY STAR SYSTEM

As expressed by Wheeler & Kipping (2019), the increase in flux seen in the light curves can be explained by a heartbeat star. Light curves for heartbeat stars in Kepler data can be found in Thompson (2012), Beck et al. (2014), and Shporer et al. (2016); they have very similar light-curve features to the ones in this work. The systems in this paper, however, are not yet identified in the Kepler binary star system catalogue Kirk et al. (2016).

A heartbeat star is a binary star system with a large eccentricity ($e \geq 0.3$) and short orbital periods (typically less than 1 yr; Fuller 2017). The shape of the light curves are dominated by tidal forces Kumar, Ao & Quataert (1995), produce pulsations, Doppler beaming, and reflections. Their light curves show a strong 'heartbeat-like' profile, hence the name. In this section, we explore binary star systems as an explanation for our 8 systems.

3.1 Binary star system model

We model a binary stellar system with interacting tidal forces, making use of the PHOEBE 2.0 PYTHON package from Jones et al. (2019). PHOEBE 2.0 is an eclipsing binary modelling code that is a complete rewrite of the original PHOEBE legacy suite written by Prša & Zwitter (2005). We use the code to generate our forward model. Prša (2011) provides an overview of the geometry used within PHOEBE 2.0. In our model, the longitude of the ascending node is arbitrarily fixed to zero. The eccentricity of the two stars is taken to be the same. The computational load to generate a light curve with PHOEBE 2.0 is very high due to the requirements to run the model, including: non-circular orbits, a Roche model to allow deformation of the star and therefore tidal effects, limb darkening, and the Kepler bandpass information. We, however, do not allow the two bodies to come close enough to be considered a contact binary system. Secondly, we do not include Doppler beaming which is difficult to accurately estimate.[1] Therefore, we perform a brute-force curve fit (instead of a Bayesian approach used later in Section 4.1, that is otherwise too computationally intensive and expensive). Using SCIPY'S 'curve_fit' function, we determine a fit to the data. The effective temperature is

[1] See the PHOEBE website http://phoebe-project.org/ for more information.

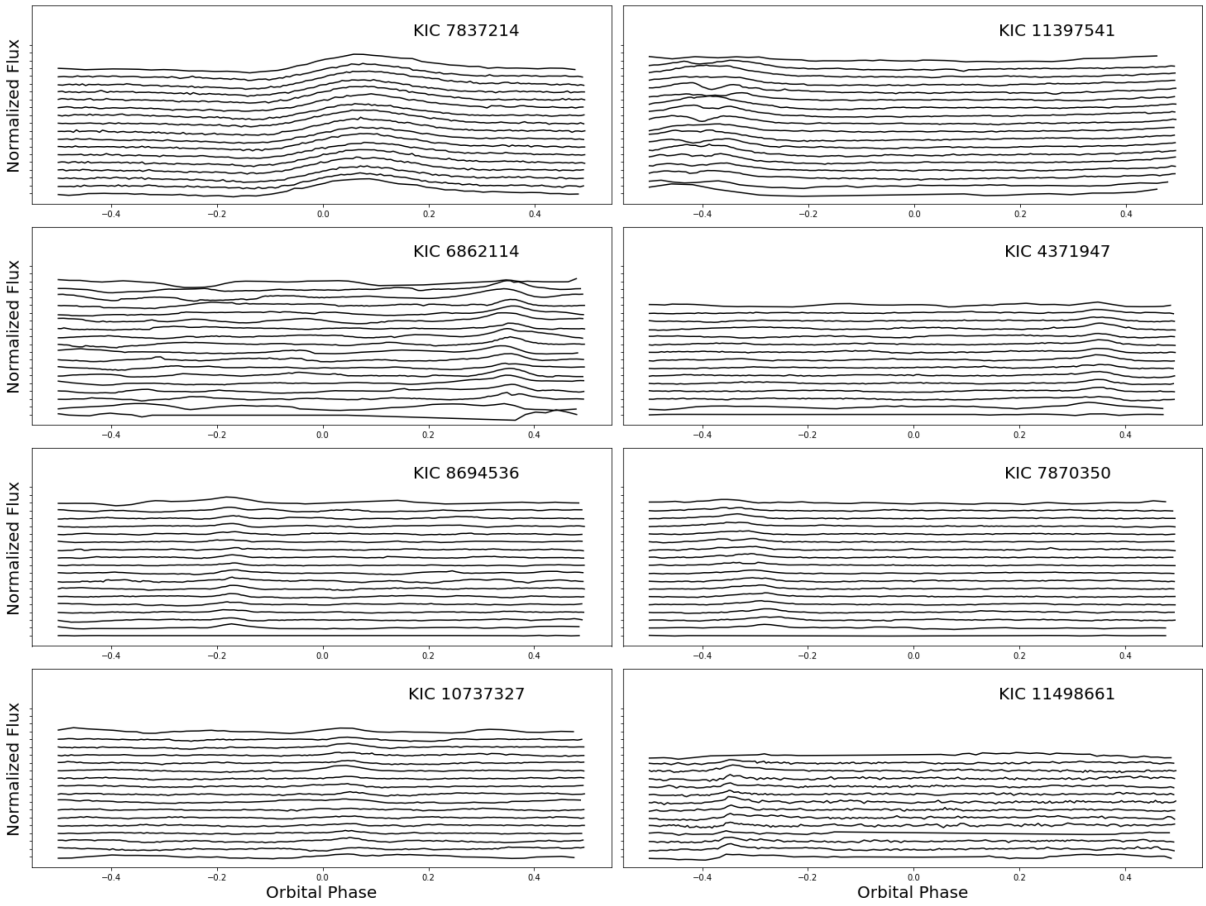

Figure 1. Stacked line plot showing all the light curves – flux as a function of orbital phase – for all available quarters for each of our OI. Each of the curves has been offset in flux by 0.000 75. The brightening in flux can be seen in each quarter individually.

taken from the Kepler catalogue Brown et al. (2011) and assume this value to be the primary's effective temperature. In the cases where no temperature is provided by Kepler, or when the Kepler value is right at the transition of stellar types, we take the value from Gaia Collaboration (2016, 2018). From the effective temperature and therefore the stellar type assuming the star is main sequence, we constrain the mass and radius of the primary star, providing the fitting routine with mid-range start values for a given stellar type. We then assume the secondary star is, first, of the same stellar type, restricting the mass, radius, and temperature. If no good fit is found, the secondary star is then assumed to be much smaller than the primary (i.e. K-type). We do this in order to minimize the effect of binary contamination. Contamination of the effective temperature from the Kepler catalogue results from the assumption that the object is a single star when it is instead an unresolved binary. The effective temperature for Kepler is valid for binary systems where the two stars are the same stellar type or the secondary is much smaller than the primary (see Pinsonneault et al. 2012). This method of fitting does not guarantee a global minimum. With tidal forces included, the main contributors to the shape of the light curve are the eccentricity, the inclination of the system, and the argument of periastron; e, i, and ω, respectively. By varying these parameters we can reproduce almost all the features seen in the various Kepler light curves. The best-fitting parameters are shown in Table 2. We note that the ability to model the light curves in Phoebe is limited due to the large parameter space and parameter degeneracies and the current lack of radial velocity data.

3.2 Results

The best-fitting curves are shown in Fig. 3. The overall shapes of the light curves are well reproduced with the binary model. Six out of the eight systems are best modelled by an F-type primary star and a K-type secondary. One system contains a G-type primary and a K-type secondary while another system requires both stars to be K-type. In some cases, there is missing flux before or after the peak itself as the curve is asymmetric such as KIC 7837214, KIC 11397514, KIC 4371947, KIC 10737327, and KIC 11498661. The asymmetry of the curves also leads to a slight overestimation of the width of the peak as seen in KIC 8694536, KIC 4371947, and KIC 10737327. The e for all but one of the systems is larger than 0.3 indicating that these could be heartbeat systems. The fitted i of all the systems are all less than 40°.

3.3 Analysis

Qualitatively, the binary system forward model does a good job reproducing the features (peak height, duration of brightening, and presence of an asymmetry) seen in the Kepler data. However, there is still overestimation and underestimation of flux. The main reason arises from the fitting function itself – we are unable to easily perform a search of the entire parameter space while at the same time there is a degeneracy between the masses and the i of the system. Within a given stellar type, small changes in the masses and radii have little effect on the light curve. The dominant changes to the shape of the

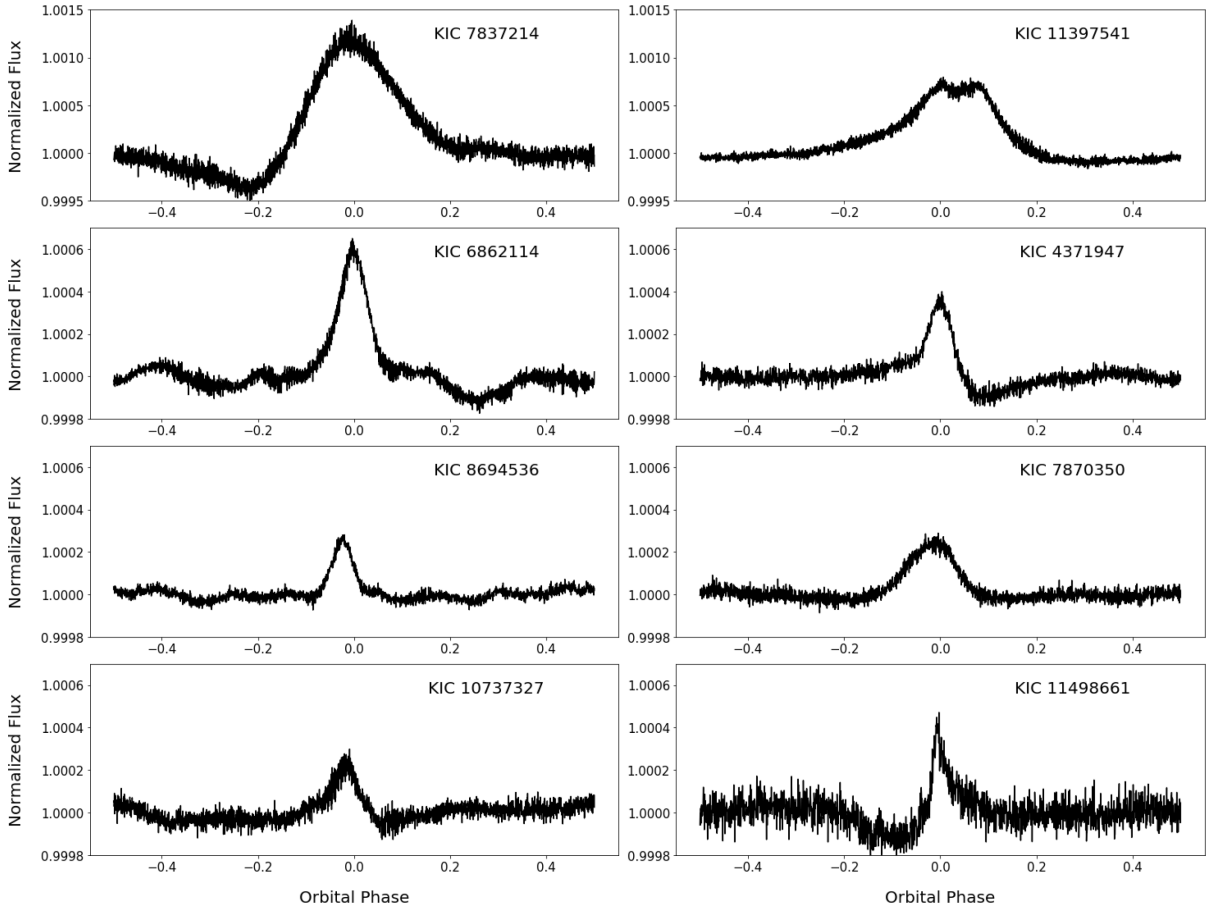

Figure 2. Folded Kepler light curves for the 8 systems showing normalized flux as a function of orbital phase. We stacked all the available Kepler quarters together and did not remove any low-frequency light-curve variations that might be associated with intrinsic stellar variability. This is done to indicate the signal-to-noise ratio of the observed brightening.

Table 2. Results from the curve fitting routine of the binary star system forward model using PHOEBE 2.0. The masses, radii, temperatures, and stellar types are given for both the primary and secondary stars indicated by $_1$ and $_2$, respectively. The primary's effective temperature (T_1) is estimated from either the Kepler or the Gaia catalogues. The eccentricity, e, and inclination, i, are assumed to be the same for both stars.

KIC ID	M_1 [$M_\odot$]	R_1 [$R_\odot$]	T_1 [K]	Stellartype$_1$	M_2 [$M_\odot$]	R_2 [$R_\odot$]	T_2 [K]	Stellartype$_2$	e	i [°]	w [°]
7837214	0.90	1.14	5774	G	0.50	0.90	4202	K	0.35	20	−170
11397541	1.10	1.20	6068	F	0.50	0.93	4460	K	0.50	25	86
6862114	1.10	1.30	7114	F	0.63	0.92	5173	K	0.62	10	50
4371947	1.10	1.20	6830	F	0.50	0.80	3975	K	0.44	37	170
8694536	1.10	1.20	6214	F	0.50	0.80	4000	K	0.55	15	170
7870350	1.10	1.30	6656	F	0.50	0.75	4000	K	0.37	34	0
10737327	1.10	1.30	6259	F	0.50	0.75	3930	K	0.35	37	35
11498661	0.75	0.95	5078	K	0.50	0.71	3917	K	0.68	35	0

brightening come from varying i, e, and w. The asymmetric dip immediately before or after the peak brightness is where we see the greatest underestimation of flux in our model. This is most-likely due to missing physics in the binary model itself. We, however, have not removed any intrinsic stellar variations in the initial data reduction. The data used here have been binned, removing some variations, making the light curves appear relatively flat but at the same time remaining stellar variations could contribute by a small amount to the observed asymmetries. Both KIC 6862114 and KIC 8694536, however, show signs of sinusoidal fluctuations of the order of 10^{-4} in flux which become more obvious when looking at the unbinned data.

These signals are similar to the tidally excited oscillations previously observed in Kepler heartbeat systems. However, this has been primarily for A-type stars that are much more massive (Guo et al. 2020) than the fitted masses in this work. The large eccentricity ($e >$ 0.5) of both these systems might increase the strength of any tidally excited oscillations, resulting in the observed variations. The physical processes happening within these systems is extreme and complex; light curves for close eclipsing binary systems often appear to have an asymmetry that is not fully understood. This is known as the O'Connell effect (O'Connell 1951) and it is possible we are seeing this in elliptical binary systems with the smallest periastron distances.

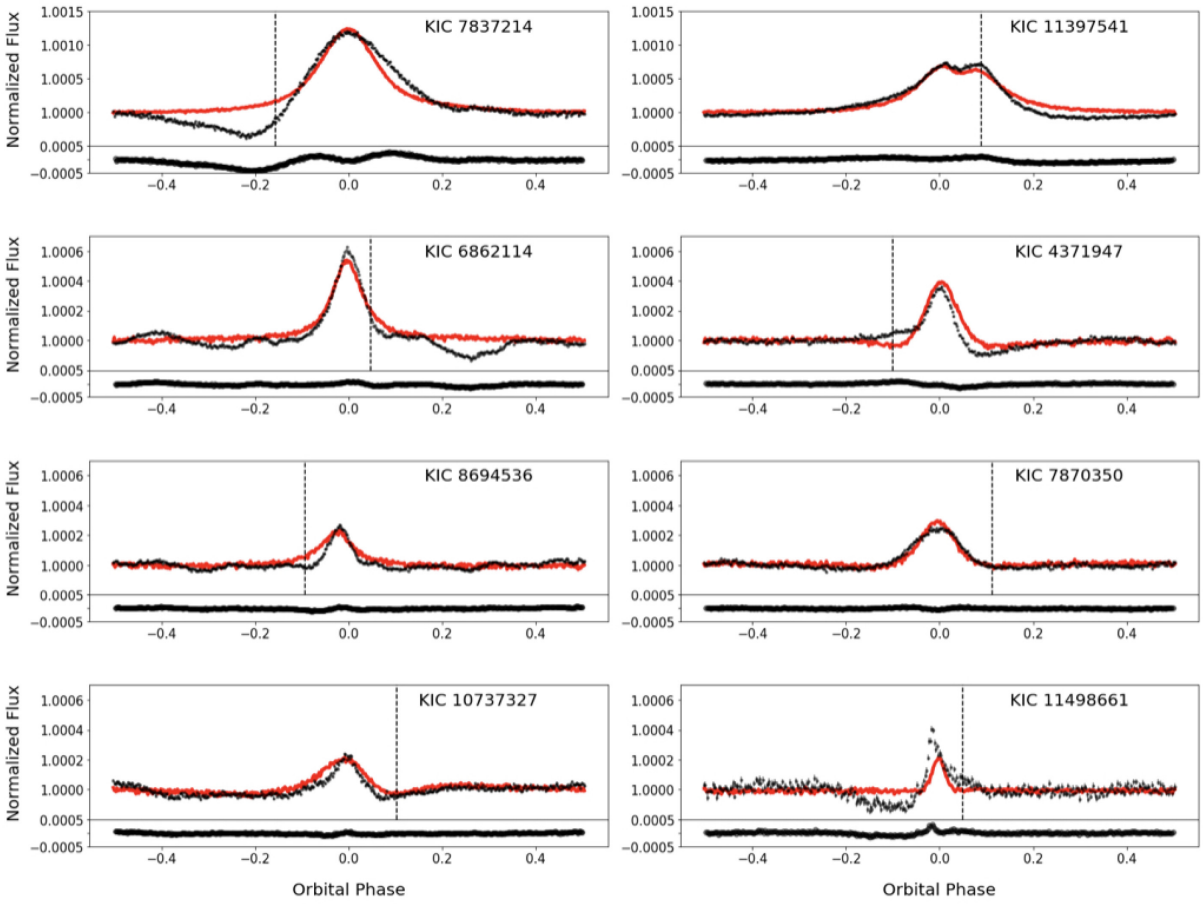

Figure 3. The resulting fits, in red, determined from standard curve fitting routine of a binary star system. Black in the top panel shows the Kepler data binned by a factor of 10 along with error bars. The vertical black dashed lines indicate the eclipse location if the system was assumed edge-on. Note that the top subplots for objects KIC 7837214 and KIC 11397541 have a different *y*-scale than the other systems. The bottom panels of each subplot show the residual and is determined simply by taking the difference between the data and the model.

4 FORWARD SCATTERING FROM OPTICALLY THIN CLOUD

The brightening of these light curves is also similar to what is observed in the Beta Pictoris light curve. The brightening seen there was explained using the scattering of a dust cloud and alternatively a comet tail by Lamers et al. (1997). In Section 1, we point out the abundance of discs at all different stages of an exoplanet's evolution and many different configurations of discs at different distances from the host star are possible. Since our objects have short orbital periods and are close-in, we expect that any gas would be blown away by stellar winds. Estimates of the equilibrium exoplanet temperature, however, indicate that any exoplanets would be cool enough (less than 1500 K; Kama, Min & Dominik 2009) to prevent sublimation of silicates, allowing for the existence of a dusty disc (see Appendix B for details). Finally, in Brogi et al. (2012), there is evidence of dust around the close-in exoplanet KIC 12557548 b that the authors attribute to disintegration. We, therefore, form a simple forward scattering model of a dust cloud and fit our model to the data.

In Fig. 4, we show a cartoon of possible system geometries resulting in the observed light curves. We consider an inclined disc of dust that enshrouds a compact object such as a planet or protoplanet. Depending on the inclination of the disc, the forward scattering occurs either before or after the inferior conjunction of the hidden body. We model the occulter as a grey dust cloud with a radial distribution consistent with the 2D Gaussian distribution which can represent many physical systems besides a grey dust cloud (e.g. grazing effects and large inclination, a gaseous exoplanet transit versus a rocky planet, or even something not due to a planet at all) and allow for a good fit of the forward scattering. By using a Gaussian in our model, we can emphasize the forward scattering and not the potential occultation (to explain the asymmetry seen in the light curves) that in itself is not sufficient to cause the brightening (and which should be a minor effect).

4.1 Simplified model

Assuming the increase in brightness is due to an optically thin disc passing in front of the host star, we can write the flux of the light curve, normalized to the star's flux, as follows:

$$\frac{f(\Theta)}{f_*} = 1 + \frac{f_{\rm sca}(\Theta)}{f_*} + \frac{f_{\rm occ}(\frac{\Theta}{2\pi})}{f_*}, \tag{1}$$

where f_* is the flux from the star and $f(\Theta)$ is the brightness variation of the system as a function of the scattering angle Θ. Taking the forward scattering flux, $f_{\rm sca}(\Theta)$, to be from an optically thin disc, we can then write it as a function of the scattering phase function, $P(\Theta)$, and the effective scattering surface for an optically thin disc $\Sigma_{\rm sca}^{\rm thin}$.

$$\frac{f_{\rm sca}(\Theta)}{f_*} = \frac{\Sigma_{\rm sca}^{\rm thin} P(\Theta)}{d^2} \tag{2}$$

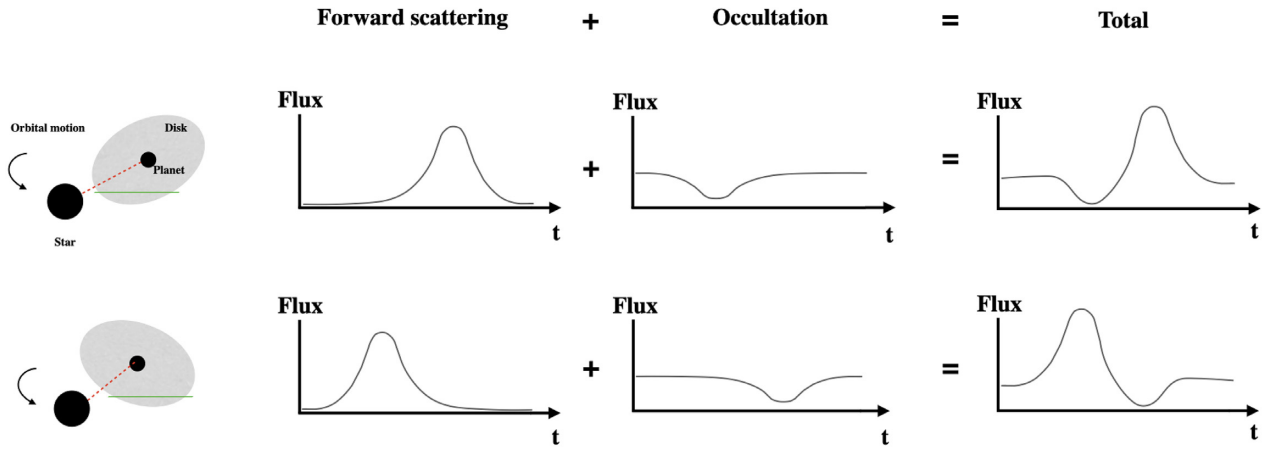

Figure 4. Diagram of the forward scattering and eclipse by a disc around a substellar companion orbiting the primary star. A star is orbited by a non-transiting substellar companion that is shrouded by a disc of dust. The long axis of the projected disk is tilted with respect to the orbital path of the companion, such that the brightening due to forward scattering of dust causes a peak in the observed flux that is offset in time with respect to the mid-point of the eclipse caused by the transit of the star behind the chord (green line) of the disk.

with d being the distance from the star to the object. We take $P(\Theta)$ to be the Henyey–Greenstein phase function

$$P(\Theta) = \frac{1}{4\pi} \frac{1 - g^2}{(1 + g^2 + 2g cos(\Theta))^{3/2}}. \quad (3)$$

Due to the geometry of the system, the scattering angle can be directly related to the orbital phase, ϕ, via $\Theta = 2\pi\phi$. The Henyey–Greenstein parameter, g, can range from -1 to 1 with values between 0 and 1 resulting in forward scattering. For completeness, we also include an occultation component in our model that might occur if there is an optical thick/grey component of the disc in the system. We fit the occultation to a Gaussian function shown in equation (4) with an amplitude A, mean phase offset (ϕ_0), and a standard deviation σ

$$\frac{f_{occ}(\phi)}{f_*} = A * \exp\left(\frac{(\phi - \phi_0)^2}{2\sigma^2}\right). \quad (4)$$

Using equation (1) as our forward model, we use a Bayesian approach to fit our model to the data using a Markov Chain Monte Carlo (MCMC) method. We make use of the PYTHON package EMCEE written by Foreman-Mackey et al. (2013), which is an implementation of an affine invariant MCMC ensemble sampler from Goodman & Weare (2010). We first estimate the distance of the object by assuming a circular orbit (see Table 3). We assume flat priors, and run 250 walkers with 1×10^5 steps all starting from different initial values. To remove contamination from the burn-in effect, we discard the first quarter. The best-fitting parameters are determined from the posterior distributions.

4.2 Results

We report the best-fitting values and their uncertainties in Table 3 and show the results of the best fit from the MCMC fitting method in Fig. 5. From the residuals shown in the figure, we see that the simplified model is in good agreement with the data. The g values all lie between 0.4 and 0.9, as expected for forward scattering. For six of the systems, the Gaussian component results in an A of the order of 10^{-4} and σ between 0.03 and 0.10. The mean phase offset is the difference in phase from the zero-point of the orbital phase. For KIC 6862114 and KIC 8694536 the values of $A \sim 10^{-10}$, meaning that the Gaussian component is not needed to fit the data and the values are reported as zeros.

4.3 Analysis

In this section, we discuss what the light curves and best-fitting parameters mean for a physical system. Although we suggest the system as seen in Fig. 4, our simple model could indeed represent many other geometries, including the solid body being indeed a third body to the star and dust cloud or disc. From the light curves in Fig. 2 we see that the brightening of the light curve due to the forward scattering of the thin disc spans 20–60 per cent of the orbital phase. The brightening is due to the scattering properties of the dust and the viewing angle of the observer. The scattering properties are represented by the g value of the Henyey–Greenstein function. For our g values, we find smaller values for smaller distances as expected from Lamers et al. (1997) and Brogi et al. (2012), with the g values increasing for larger distances. The g value can also be used as a tracer for the type of dust causing the forward scattering. The effective scattering surface areas required for the observed brightening events are not significantly large and the radii of the required optically thin discs for a given surface area are smaller than the Hill sphere radius of the system (see Appendix A for more details).

For the occultation due to our Gaussian term, we look at the σ reported in Table 3. The duration of dip due to the grey dust should span no more than 1/6-th the orbital phase. Using the σ in Table 3, we find the full-width-half-maximum (FWHM; an estimation of the dip duration) for KIC 787214, KIC 7870350, and KIC 10737327 all are much larger than 1/6-th the orbital phase. Assuming we have an exoplanet at the center of the disc, the exoplanet's mass necessary to have such a large Hill sphere radius such that the dust can span such a large portion of the orbit would result in an exoplanet of approximately 16 M_J. We estimate this value by taking the Hill sphere radius to be 1/6-th the orbit; assuming the host star to be one solar mass, we solve for the secondary mass, m (i.e. $0.17 = (\frac{m}{3*1M_J})^{1/3}$). Such a large exoplanet (or brown dwarf) would change the observed light curve for the short orbital periods of our 8 systems. More specifically, the transit depth would be approximately 1 per cent and not the observed 0.1–0.3 per cent. Therefore objects with FWHM larger than 1/6-th must either be modelled by a second Henyey–Greenstein phase function with a g value less than 0, or be heartbeat binary stars. KIC 4371947 and KIC 11498661 have FWHMs just under 1/6-th the orbital phase while the FWHM of the other systems are much smaller.

Table 3. The different model parameters as determined by MCMC fit. The distance, d, is determined from assuming a circular orbit and given as input into the forward model. The fitted parameter is the 50th percentile of the samples in the marginalized distributions, while the uncertainties are determined from the 16th and 84th. If $A < 10^{-10}$, we simply report it as zero, and the contribution from the Gaussian is negligible.

KIC ID	d [au]	$a_{\rm thin}$ [R_s^2]	g	ϕ_0	σ	A
7837214	0.073	$0.925^{+0.024}_{-0.026}$	$0.434^{+0.005}_{-0.005}$	$-0.199^{+0.004}_{-0.004}$	$0.097^{+0.003}_{-0.003}$	$5.263\text{E-}4^{+1.317\text{E-}5}_{-1.436\text{E-}5}$
11397541	0.112	$1.066^{+0.023}_{-0.024}$	$0.577^{+0.001}_{-0.001}$	$0.031^{+0.001}_{-0.001}$	$0.025^{+0.000}_{-0.000}$	$4.657\text{E-}4^{+5.495\text{E-}5}_{-5.769\text{E-}5}$
6862114	0.195	$1.263^{+0.047}_{-0.048}$	$0.773^{+0.005}_{-0.005}$	0.	0.	0.
4371947	0.161	$0.533^{+0.145}_{-0.191}$	$0.771^{+0.024}_{-0.021}$	$0.061^{+0.015}_{-0.019}$	$0.069^{+0.011}_{-0.007}$	$1.527\text{E-}4^{+2.34\text{E-}5}_{-3.614\text{E-}5}$
8694536	0.218	$0.234^{+0.023}_{-0.025}$	$0.842^{+0.010}_{-0.009}$	0.	0.	0.
7870350	0.170	$1.853^{+0.536}_{-0.818}$	$0.551^{+0.039}_{-0.038}$	$-0.019^{+0.008}_{-0.008}$	$0.129^{+0.008}_{-0.013}$	$1.594\text{E-}4^{+5.598\text{E-}5}_{-8.240\text{E-}5}$
10737327	0.161	$0.215^{+0.065}_{-0.091}$	$0.721^{+0.036}_{-0.035}$	$0.004^{+0.01}_{-0.016}$	$0.095^{+0.011}_{-0.011}$	$1.130\text{E-}4^{+2.909\text{E-}5}_{-3.967\text{E-}5}$
11498661	0.212	$0.215^{+0.032}_{-0.039}$	$0.790^{+0.017}_{-0.016}$	$-0.047^{+0.002}_{-0.004}$	$0.066^{+0.005}_{-0.005}$	$1.817\text{E-}4^{+1.629\text{E-}5}_{-1.894\text{E-}5}$

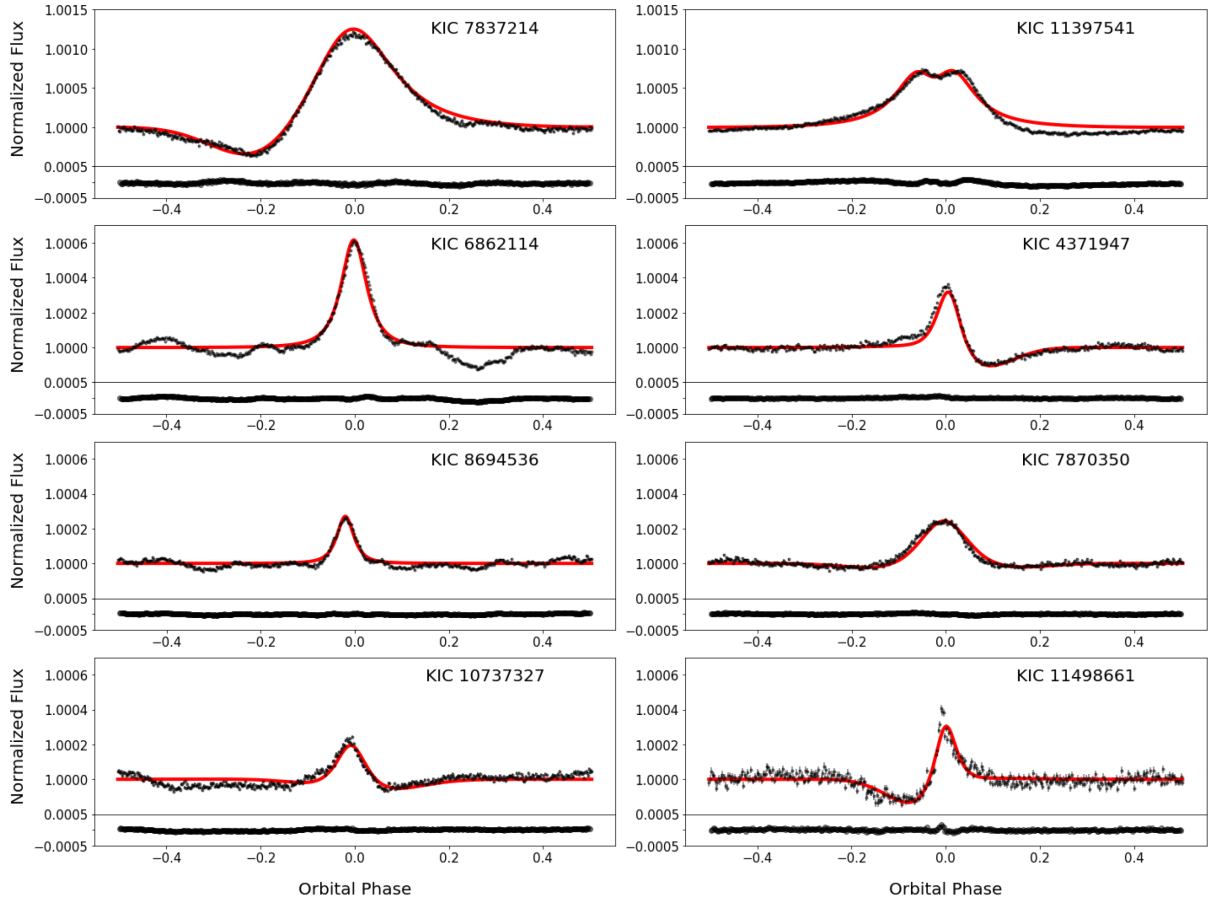

Figure 5. The resulting fits, in red, determined from the posterior distribution of the MCMC fit. Black in the top panel shows the Kepler data binned by a factor of 10 along with error bars. Note that the top plots for objects KIC 7837214 and KIC 11397541 have a different y-scale than the other systems. The bottom panels of each subplot show the residual, which is determined by simply taking the difference between the data and the model.

5 DISCUSSION AND COMPARISON OF THE TWO MODELS

In Section 3, we apply an eccentric binary star-system model and present results of fitting it to the data. All the systems require an $e > 0.3$. This, in combination with the short orbital periods, indicates the observed light curves can be explained by current heartbeat system models. However, Fig. 3 shows that although the binary model does a good job of reproducing the overall shape of the light curves, there is still a flux mismatch in many cases – most notably, KIC 783714, KIC 4371947 KIC 8694536, and KIC 11498661. Due to the degeneracy of the masses and the inclination, the curve fitting algorithm does not find a solution that perfectly matches the observed curves. In combination with the difficulties in modelling close binaries and certain physical processes (such as flow of material between the two objects at closest approach and Doppler beaming) missing from the model itself, the flux discrepancy is in itself not sufficient to rule out these being true binary systems.

While the simple heartbeat model is a good fit for all eight of the systems, we consider a model that includes forward scattering from an optically thin disc of dust surrounding a non-transiting exoplanet that is orbiting the host star in Section 4. A circumsecondary disc that is tilted with respect to the path of the planet's orbit will produce a forward scattering peak, but that is then offset in time with respect to the transit of the star behind a chord across the dust disc (see Fig. 4). Our scattering model provides a good fit to the data, see Fig. 5, and provides a qualitatively better explanation for some objects than the binary system. From Table 3, we note that the uncertainties (the 18th and 84th percentiles) reveal that $a_{\rm thin}$ is not well constrained by the data for KIC 4371947 and KIC 7870350. There is a degeneracy between the scattering surface area and the amplitude of the Gaussian component. Despite these limitations, the simplified model shows that with forward scattering, we can obtain the amplitude and duration of the brightening seen in all of our light curves.

The Gaussian component σ is too large, indicating that a 16 M_J exoplanet would be needed to allow for the dust to span such a large portion of the orbit, for three of the systems: KIC 787214, KIC 7870350, and KIC 10737327. Given the features of the light curves, we see no evidence for the existence of such a massive exoplanet. While it is possible to create more complex dust models that we could fit to the data, we expect these objects to indeed be heartbeat stars. The remaining five could be described by either model. For KIC 6862114 and KIC 8694536, the brightening is symmetric and does not require any occultation, indicating that inclination of the system would have to be large such that the exoplanet would not pass in front of the star. For the other three systems, the model provides physically realistic values for both a companion and the disc.

Radial velocity measurements would further enable the type of system to be identified, as well as provide mass constraints for the systems. For KIC 787214, KIC 7870350, and KIC 10737327, for which the disc model is not able to describe the system, radial velocity measurements would confirm them as heartbeat systems. Assuming an eccentric binary system, the binary mass function can be written as in equation (5)

$$f = \frac{M_2^3 sin^3 i}{(M_1 + M_2)^2} = \frac{P_{orb} K^3}{2\pi G}(1 - e^2)^{3/2} \quad (5)$$

K is the semi-amplitude of radial velocity curve and is related to the velocity of the largest object and the geometry of the system. Rearranging equation (5) for K, we estimate the peak of the radial velocity signal with the values in Table 2 to be 6–21 km s^{-1}. In the case of the optically thin cloud, we would expect a very low peak velocity. Therefore, radial velocity data would be sufficient to distinguish which physical model is responsible for observed light curves. For the five objects that could be optically thin discs we would also expect a polarization signal. Due to the closeness of the expected disc to the host star, any polarized light from the disc itself would not be angularly resolved with an instrument such as VLT/SPHERE's (Beuzit 2019) polarization subsystem ZIMPOL (Schmid et al. 2018). Since the star itself is unpolarized, any polarized light could be attributed to the disc. With such data of the system in combination with radiative transfer models, it is possible to put constraints on the dust mass.

6 CONCLUSION

In this paper, we investigate eight systems identified in the Kepler data. We find that most of the light curves can be explained by a heartbeat binary star system with an F-type primary and a K-type companion. We do, however, see a discrepancy of flux for the asymmetric part of the light curves. While this could be due to physics not included in the heartbeat models, we also investigate whether the light curves can be explained by a simple forward scattering model composed of an optically thin disc of dust surrounding a non-transiting exoplanet. We determine that five out of the eight observed light curves could be described in this manner. Further investigation of KIC 11397541, KIC 6862114, KIC 4371947, KIC 8694536, and KIC 11498661 using radial velocity and polarization measurements will therefore be needed to determine if they are heartbeat systems or dust clouds around an exoplanet. Follow-up radial velocity observations of KIC 787214, KIC 7870350, and KIC 10737327 could further be used to confirm them as heartbeat systems.

ACKNOWLEDGEMENTS

This paper includes data collected by the Kepler mission. Funding for the Kepler mission is provided by the NASA Science Mission directorate. The authors thank the PHOEBE discussion mailing list for helpful input, and thank Leiden University, NOVA, METIS consortium, and TNO for funding this research.

This work has made use of data from the European Space Agency (ESA) mission *Gaia* (https://www.cosmos.esa.int/gaia), processed by the *Gaia* Data Processing and Analysis Consortium (DPAC, https://www.cosmos.esa.int/web/gaia/dpac/consortium). Funding for the DPAC has been provided by national institutions, in particular the institutions participating in the *Gaia* Multilateral Agreement.

DATA AVAILABILITY

The data used in this paper is from the *Kepler Space Telescope* and can be found at the Mikulski Archive for Space Telescopes (MAST) which is hosted by the Space Telescope Science Institute (STScI).

REFERENCES

Andrews S. M. et al., 2018, ApJ, 869, L41
Ansdell M. et al., 2016, ApJ, 816, 69
Beck P. G. et al., 2014, A&A, 564, A36
Beuzit J.-L. et al., 2019, A&A , 631, A155
Borucki W. J. et al., 2010, Science, 327, 977
Brogi M., Keller C. U., de Juan Ovelar M., Kenworthy M. A., de Kok R. J., Min M., Snellen I. A. G., 2012, A&A, 545, L5
Brown T. M., Latham D. W., Everett M. E., Esquerdo G. A., 2011, AJ, 142, 112
Christiaens V., Cantalloube F., Casassus S., Price D. J., Absil O., Pinte C., Girard J., Montesinos M., 2019, ApJ, 877, L33
Christiansen J. L. et al., 2012, PASP, 124, 1279
De Cat P., Aerts C., De Ridder J., Kolenberg K., Meeus G., Decin L., 2000, A&A, 355, 1015
Foreman-Mackey D., Hogg D. W., Lang D., Goodman J., 2013, PASP, 125, 306
Fuller J., 2017, MNRAS, 472, 1538
Gaia Collaboration, 2016, A&A, 595, A1
Gaia Collaboration, 2018, A&A, 616, A1
Goodman J., Weare J., 2010, Commun. Appl. Math. Comput. Sci., 5, 65
Guo Z., Shporer A., Hambleton K., Isaacson H., 2020, ApJ, 888, 95
Isella A., Benisty M., Teague R., Bae J., Keppler M., Facchini S., Pérez L., 2019, ApJ, 879, L25
Jones D. et al., 2020 , ApJS, 247, 63
Kama M., Min M., Dominik C., 2009, A&A, 506, 1199
Kirk B. et al., 2016, AJ, 151, 68
Kobayashi H., Kimura H., Watanabe S.-I., Yamamoto T., Müller S., 2011, Earth Planets Space, 63, 1067

Kumar P., Ao C. O., Quataert E. J., 1995, ApJ, 449, 294
Lamers H. J. G. L. M., Lecavelier Des Etangs A., Vidal-Madjar A., 1997, A&A, 328, 321
Lecavelier des Etangs A. et al., 2017, A&A, 603, A115
Lightkurve Collaboration, 2018, Astrophysics Source Code Library, record ascl:1812.013
O'Connell D. J. K., 1951, Riverview College Observatory Publications, 2, 85
Pinsonneault M. H., An D., Molenda-Zakowicz J., Chaplin W. J., Metcalfe T. S., Bruntt H., 2012, ApJS, 199, 30
Prša A., 2011, Villanova University, College of Arts and Sciences, Department of Astronomy and Astrophysics, Available at: http://phoebe-project.org/static/legacy/docs/phoebe_science.pdf
Prša A., Zwitter T., 2005, ApJ, 628, 426
Ricker G. R. et al., 2015, J. Astron. Telesc. Instrum. Syst., 1, 014003
Schmid H. M. et al., 2018, A&A, 619, A9
Shporer A. et al., 2016, ApJ, 829, 34
Smith J. C. et al., 2012, PASP, 124, 1000
Thompson S. E. et al., 2012, ApJ, 753, 86
Welsh W. et al., 2011, ApJS, 197 , 4
Wheeler A., Kipping D., 2019, MNRAS, 485, 5498

APPENDIX A: EFFECTIVE SCATTERING AREA AND DISC SIZE ESTIMATION

In Section 4, the forward scattering of an optically thin disc is fit to the observed Kepler data. One parameter estimated by the fit is the projected effective scattering area, $\Sigma_{\rm sca}^{\rm thin}$. From this we can estimate the radius of a thin circular disc with the same effective area using the following equation:

$$\Sigma_{\rm scat}^{\rm thin} = \int_0^r (1 - {\rm e}^{-\tau_{sca}(p)})(\pi\, p){\rm d}p, \tag{A1}$$

where $\tau(p)$ is the optical depth along the line of sight through the cloud. Assuming an average optical depth over the entire optically thin disc, the equation becomes

$$\Sigma_{\rm sca}^{\rm thin} = (1 - {\rm e}^{-\tau_{sca}})\pi r^2. \tag{A2}$$

In Table A1, we report the radii for two different values of τ. We estimate the Hill sphere radius for a $1\,{\rm M}_J$ exoplanet in a circular orbit around an $1\,{\rm M}_\odot$ star with the periods reported in Table 1. For reference, the Hill sphere radius of the hot Jupiter HD 209458 b is 0.003 au with an orbital period of 3.5 d and a mass of $0.71\,{\rm M}_J$ (Lecavelier des Etangs et al. 2017). In all cases of $\tau = 0.5$, the radii are smaller than the estimated Hill sphere radii, while for $\tau = 0.1$ most are too large. However, these values do indicate that projected surface scattering areas found are realistic values.

APPENDIX B: EQUILIBRIUM TEMPERATURE

In our optically thin model, we assume the presence of a dusty disc with an exoplanet. Close into the host star, gas has most-likely been blown away by stellar winds. For dust to exist, however, the grains must be below their sublimation temperature. Sublimation temperature of dust differs depending on the dust composition. For example, carbon has a high sublimation temperature of 2000 K (Kobayashi et al. 2011) while silicates sublimates at 1500 K (Kama et al. 2009). We assume the composition of our dust disc to be silicates. We therefore estimate the temperature of the dusty gains by determining the equilibrium temperature of an exoplanet orbiting at that The equilibrium temperature, $T_{\rm eq}$ of an exoplanet orbiting around its host star is given by

$$T_{\rm eq} = T(1 - \alpha)^{0.25}(r/2a)^{0.5} \tag{B1}$$

with T being the stellar temperature, r being the stellar radii, and α as the exoplanet's albedo. We then take the stellar temperature from Table 2 and estimate r from the stellar type. Therefore, assuming a blackbody ($\alpha = 0$), the upper limits for $T_{\rm eq}$ for our systems ranges from 500 to 1100 K. These values are below the sublimation temperature for silicate.

Table A1. Estimation of $r_{\rm sca}^{\rm thin}$ for two different values of τ: 0.5 and 0.1. An estimation of the Hill sphere radius is made from a $1\,{\rm M}_J$ exoplanet in a circular orbit around a $1\,{\rm M}_\odot$ star.

KIC ID	$a_{\rm thin}[R_s^2]$	$r_{\rm sca}^{\rm thin}$[au] : $\tau = 0.5$	$r_{\rm sca}^{\rm thin}$[au] : $\tau = 0.1$	Hill sphere radius [au]
7837214	0.925	0.004	0.014	0.005
11397541	1.066	0.004	0.016	0.008
6862114	1.263	0.005	0.019	0.013
4371947	0.533	0.003	0.008	0.011
8694536	0.234	0.002	0.004	0.014
7870350	1.853	0.006	0.028	0.012
10737327	0.215	0.002	0.003	0.011
11498661	0.215	0.002	0.003	0.017

This paper has been typeset from a TEX/LATEX file prepared by the author.